Supplementary Material:

Gold rotor bead tracking for high-speed measurements of DNA twist, torque, and extension

Paul Lebel[1,2], Aakash Basu[1,2,5], Florian C. Oberstrass[2], Elsa M. Tretter[3,5], and Zev Bryant[2,4]

[1] Department of Applied Physics, Stanford University, Stanford, California, USA

[2] Department of Bioengineering, Stanford University, Stanford, California, USA

[3] Department of Molecular and Cell Biology, University of California, Berkeley, California, USA

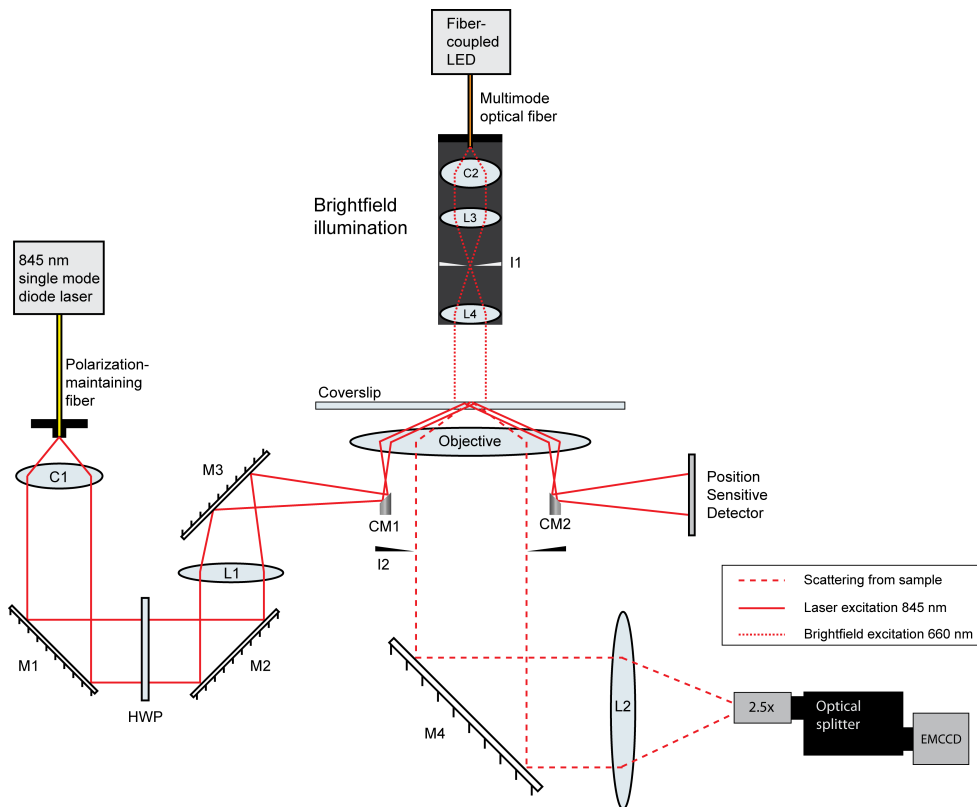[4] Department of Structural Biology, Stanford University Medical Center, Stanford, California, USA

[5] Present addresses: Howard Hughes Medical Institute and Laboratory of Sensory Neuroscience, The Rockefeller University, New York, New York, USA (A.B.) and Nurix Inc., San Francisco, California, USA (E.M.T.).

Correspondence should be addressed to Z.B. (zevry@stanford.edu)

Contents

Supplementary Figure 1. Overall optical schematic.

Linearly polarized light from a fiber-coupled 845 nm single mode laser diode was collimated (C1) into a ~2 mm beam and focused onto the objective's back focal plane via a small 45° coupling mirror (CM1, see also **Fig. 1a** and **Supplementary Fig. 2**). A half-wave plate (HWP) was oriented to obtain s-polarization at the sample interface. The laser was brought to a focus with a 500 mm achromatic lens (L1), such that a ~13 μm diameter beam was totally internally reflected at the sample's glass/water interface. The reflected beam was then extracted from the imaging path via a second 45°mirror (CM2), and collected on a position-sensitive detector for the purpose of focal plane stabilization (**Methods, Supplementary Fig. 9**). Scattered light from rotor beads was reflected from an ultraflat mirror (M4) and imaged with lens L2 into a 2.5X relay unit through an optical splitter (**Supplementary Fig. 3a**), and finally onto an EMCCD camera. An iris (I2) was positioned underneath the objective holder in order to block stray light. During force calibrations, the same imaging path was used to acquire brightfield images of magnetic beads, illuminated using a homebuilt path that employs an iris (I1) to reject off-axis rays for improved collimation. See **Supplementary Note 3** for a complete parts list.

Supplementary Figure 2. Mechanical drawing of the objective holder for evanescent darkfield imaging.
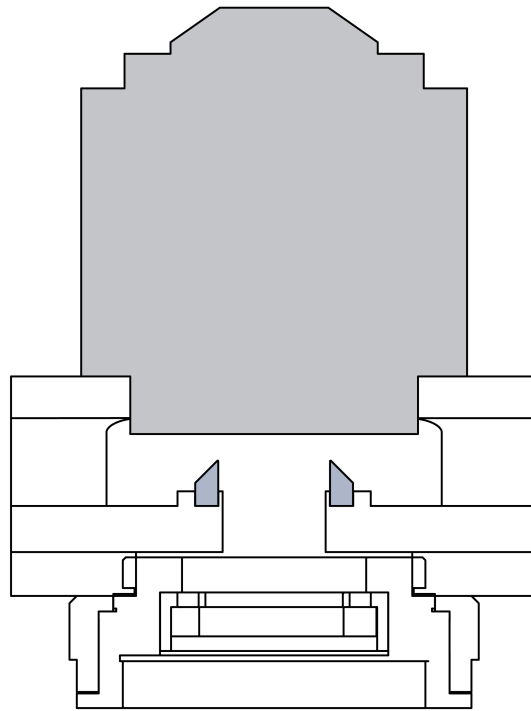
A cross-section illustrates the design for positioning small mirrors that couple light into and out of the objective. The two mirrors were glued into machined aluminum sliders, which fit with tight tolerances into complimentary slots in the objective holder, and could be moved radially in and out of the back focal plane. An adjustable iris was attached via underside threads in order to reject stray light.

Supplementary Figure 3. Calibration of the evanescent field decay constant.
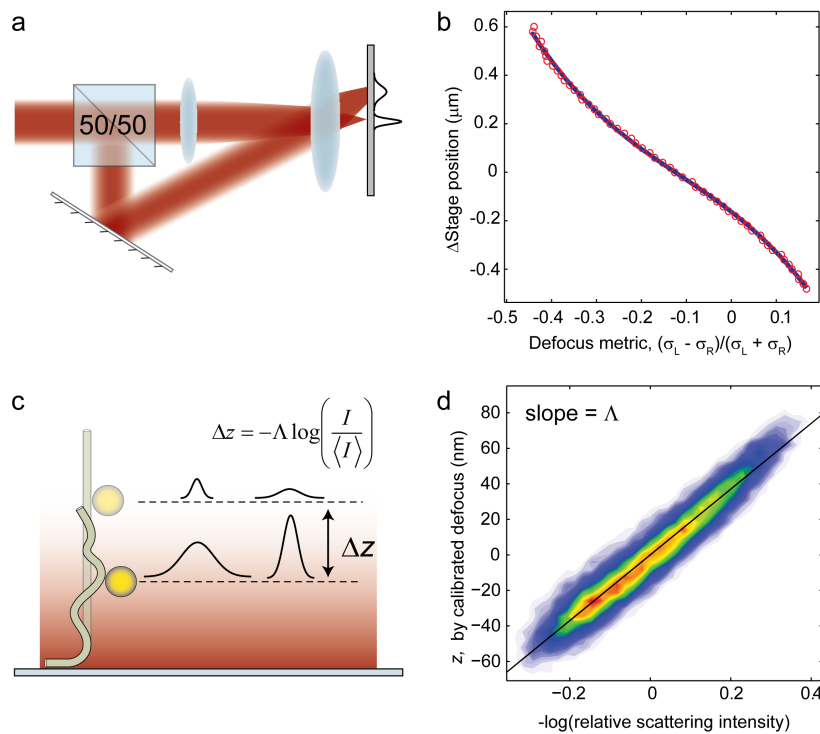
The decay constant of the evanescent field was calibrated to stepping motion of the piezoelectric stage, via cross-correlation with a variant of dual-focus imaging[1] (DIO). The procedure comprised two steps: (1) calibration of DIO to motion of the stage, and (2) correlation of intensity fluctuations with the calibrated DIO signal. **(a)** Simplified schematic of the dual-focus imaging path. A 50/50 beamsplitter was used to split the image path for DIO, and a 300 mm lens was inserted in one path to create a relative focal shift between the two paths, which were imaged side-by-side on the same camera sensor. **(b)** Calibration curve relating vertical motion of the piezo stage to the signal generated by DIO. An empirical defocus metric was computed as the difference of image pixel intensity standard deviations, normalized by their sum. A cubic polynomial was fit to the data, which served to convert dual-focus data into z-height after correcting for the focal shift (0.84) due to the refractive index mismatch between the immersion oil and sample buffer, determined as reported earlier[2,3]. **(c)** Schematic depicting how vertical motion of the probe generates correlated intensity and DIO signals: changes in scattering intensity occur simultaneously with changes in focus. Hypothetical image planes separated by Δz are shown as dashed lines. **(d)** A 2D histogram of -log(scattering intensity) versus z, as measured by DIO. The rotor bead was imaged under low tension (< 0.1 pN) in order to allow large z-fluctuations. The slope of the fit to the distribution equals the decay constant Λ, which typically ranged between 130-200 nm (shown here: Λ = 185 nm). Repeated calibrations on the same molecule yielded ~6% variability in the measured decay constant.

Supplementary Figure 4. Angular noise power spectral density.
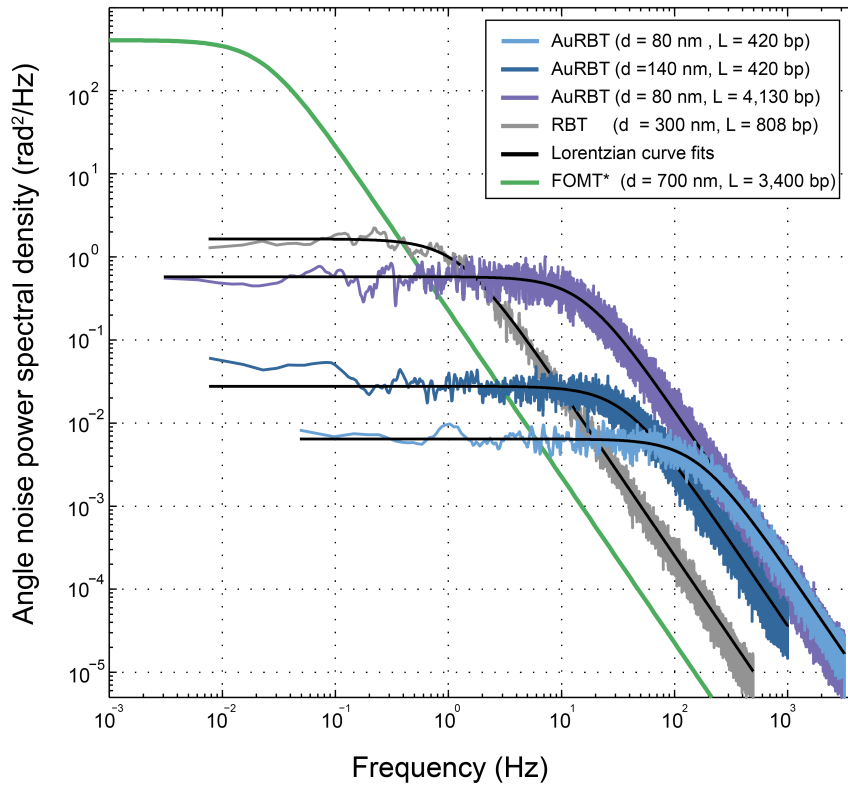
Angular noise power spectral densities are shown for the same datasets displayed in **Figure 2a**. Solid lines show fits to the expected Lorentzian function[4]:

$$S = \frac{k_B T}{\pi^2 \gamma \left(f^2 + f_c^2 \right)} \tag{S1}$$

The corner frequency is given by $f_c = \kappa / (2\pi\gamma)$, where κ is the torsional spring constant of the DNA tether and γ is the rotational drag of the rotor bead. Fit parameters are shown in **Supplementary Table 1**, along with the limiting low-frequency power spectral density,

$$S\big|_{f \ll f_c} \approx \frac{4 k_B T \gamma}{\kappa^2} = \frac{4 k_B T}{\kappa^2} \left(14\pi\eta r^3 \right) \tag{S2}$$

*FOMT theoretical power spectral density was calculated using the most favorable parameters reported in reference[5].

Supplementary Figure 5. Expected effect of surface proximity on effective rotational drag.
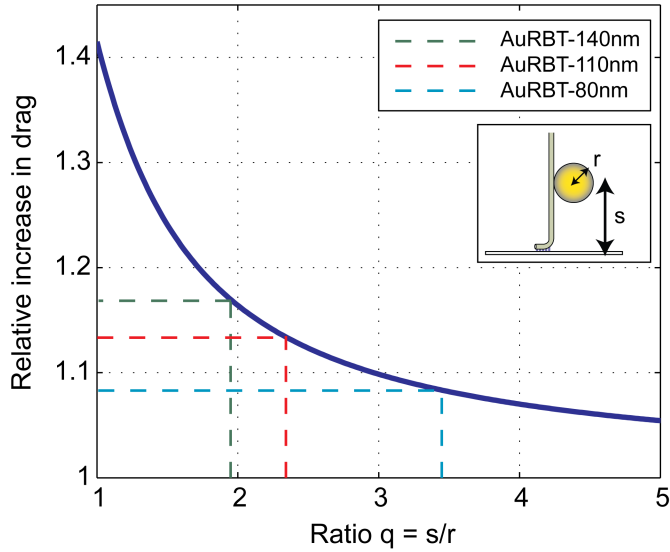
Power series expansions of Faxen's corrections[6] were used to predict the increased effective viscosity in the presence of the nearby coverslip. The expansion was in terms of the ratio of a particle's separation from the surface, *s,* to its radius, *r.* For rotor beads, the increase in drag may be separated into rotational and translational correction factors[6], which modify the formula for rotational drag about an axis tangent to the spherical particle's surface:

$$\gamma = C_{rot}8\pi\eta r^3 + C_{trans}6\pi\eta r^3 \tag{S3}$$

$$C_{rot} \approx \frac{1}{1 - \left(\frac{1}{8}\right)q^{-3}}$$

$$C_{trans} \approx \frac{1}{1 - \left(\frac{9}{16}\right)q^{-1} + \left(\frac{1}{8}\right)q^{-3}}$$

$$q \equiv \frac{s}{r}$$

The overall relative increase in rotational drag for a rotor bead near a surface (plotted above) is then given by:

$$\frac{\gamma}{14\pi\eta r^3} \approx \left(\frac{1}{14}\right)(8C_{rot} + 6C_{trans})$$

Dashed lines indicate the ratio *q* = *s/r* and the corresponding predicted correction magnitude for each of the three bead sizes and their corresponding tether lengths (all in the ~400 bp range) used in this study, for the approximation in which the molecule is 100% extended. The estimated corrections are in reasonable agreement with our experimental determination of rotational diffusion constants (see main text **Fig. 2c**): a cubic fit to the combined dataset resulted in an effective viscosity of 1.2 mPa s, approximately 20% higher than the expected bulk viscosity at 20°C [7].

Supplementary Figure 6. Torque noise power spectral density.
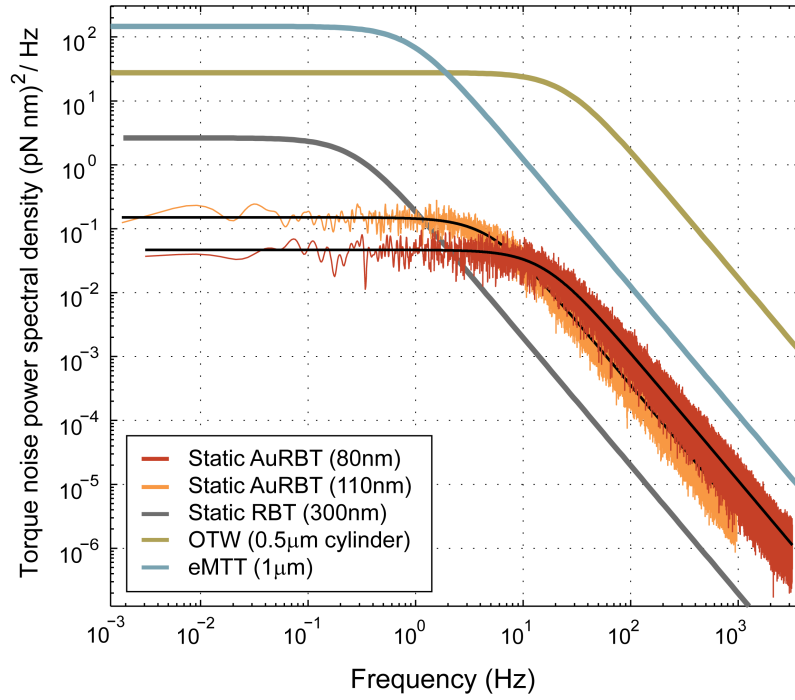
Static AuRBT and static RBT measure torque via the deflection of a calibrated torsional spring. The power spectral density of measured torques is[8]:

$$S_\tau = \frac{\kappa^2 k_B T}{\pi^2 \gamma \left(f^2 + f_c^2 \right)} \tag{S4}$$

$$\left. S_\tau \right|_{f \ll f_c} \approx 4 k_B T \gamma = 56 k_B T \pi \eta r^3 \tag{S5}$$

Data and Lorentzian fits are shown for the same datasets as **Fig. 5**, together with theoretical curves using reported parameters for a variety of existing techniques: OTW[8-12] (parameters from reference [8]), eMTT[13], and static RBT[14,15].

Supplementary Figure 7. Precision and accuracy of angular tracking.
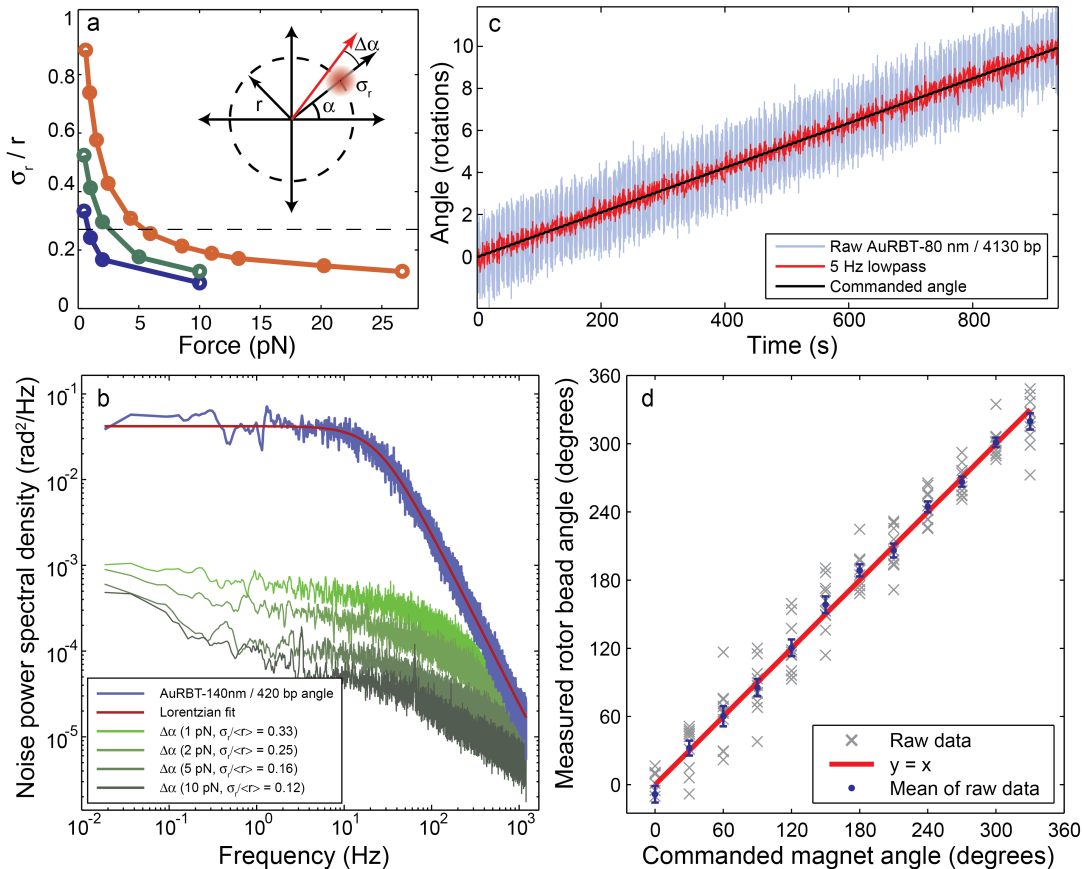
(a,b) Angular precision: measured angles are determined from the xy position of the rotor (main text **Fig. 1b**) and include a contribution from positional error σ_r (a, inset) arising from lateral DNA fluctuations and imaging noise. (a) σ_r as a function of force was measured for three different assays (blue, AuRBT-140nm; green, AuRBT-110nm; orange, AuRBT-80nm). Data points represent the normalized standard deviation in the measured orbital radius for full-bandwidth acquisition. For error-free angle tracking (defined as showing fewer than ~10-20 spurious angle jumps per million frames), AuRBT requires that forces are high enough to restrict lateral fluctuations below an empirically-determined threshold, $\sigma_r / r < 0.27$ (dashed line); at this threshold, the resulting full-bandwidth angle determination error is ± ~15°. (b) Power spectral density of the total angular noise (blue, acquired at 10 pN) and of a predicted contribution to angular noise from localization error at different forces (shades of green) for AuRBT-140nm/420 bp. Measured deviations Δr from mean orbital radius r were used to determine the scale of lateral fluctuations, and converted into predicted angular errors (shades of green) using $\Delta\alpha=\tan^{-1}(\Delta r / r)$. For this molecule, the 1 pN condition lies just below the trackability threshold. Position noise contributes negligibly at relevant frequencies, up to well beyond the angular corner frequency. (c,d) Assessment of angle-tracking accuracy. AuRBT-80nm/4130bp (top-constrained molecules as in **Fig. 3a**) was rotated through a total of ten turns by stepping the magnets in 30° increments; angular data were acquired for 30,000 frames at each position. (d) Analysis of the raw data in (c). Gray markers show the mean measured angle at each physical dwell, collapsed onto [0, 360°]; the averaged angle data are shown in blue as mean ±

s.e.m. The measured rotor angle accurately reflects the commanded angle to within the precision of the measurement, with an RMSD of 6°.

Supplementary Figure 8. Axial resolution of AuRBT.
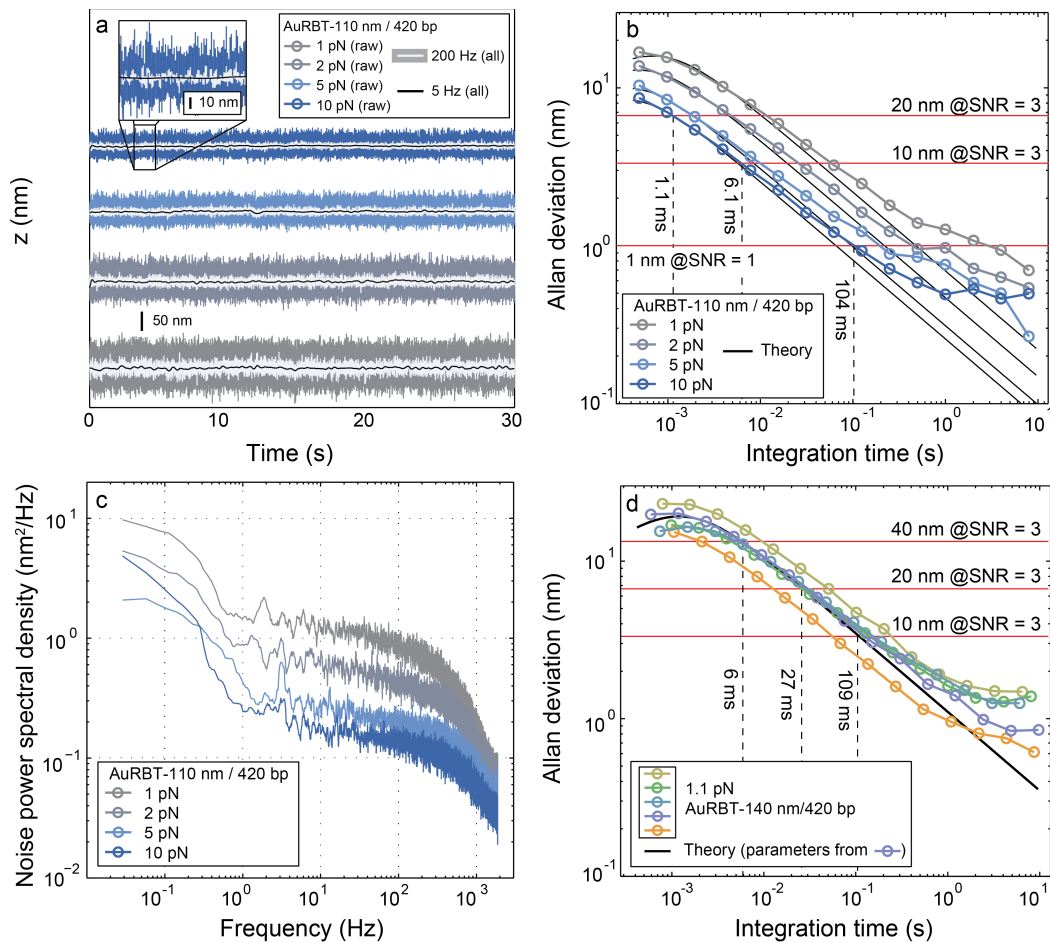
(a-c) Axial fluctuations for the AuRBT-110nm/420bp assay observed with evanescent nanometry (EN) over a range of tensions. **(a)** Raw traces are overlaid with 200 Hz and 5 Hz lowpass filtered data. **(b)** The Allan deviation (a common measure of noise for signals that include drift[16]) was computed as a function of integration time for the datasets represented in **(a)** and overlaid with theory[16], using parameters estimated from Lorentzian fits to the noise power spectra. Drift leads to deviations from theory at long timescales. Vertical lines indicate the integration times required to reduce the Allan deviation below the indicated thresholds. **(c)** EN noise power spectral densities are shown for the same data used in **(b)**. **(d)** Allan deviations for several AuRBT-140nm/420bp molecules, representative of the conditions used for gyrase experiments (**Fig. 4**). Molecules were held under 1.1 pN and imaged in gyrase buffer.

Supplementary figure 9. Drift rejection and focal stabilization.
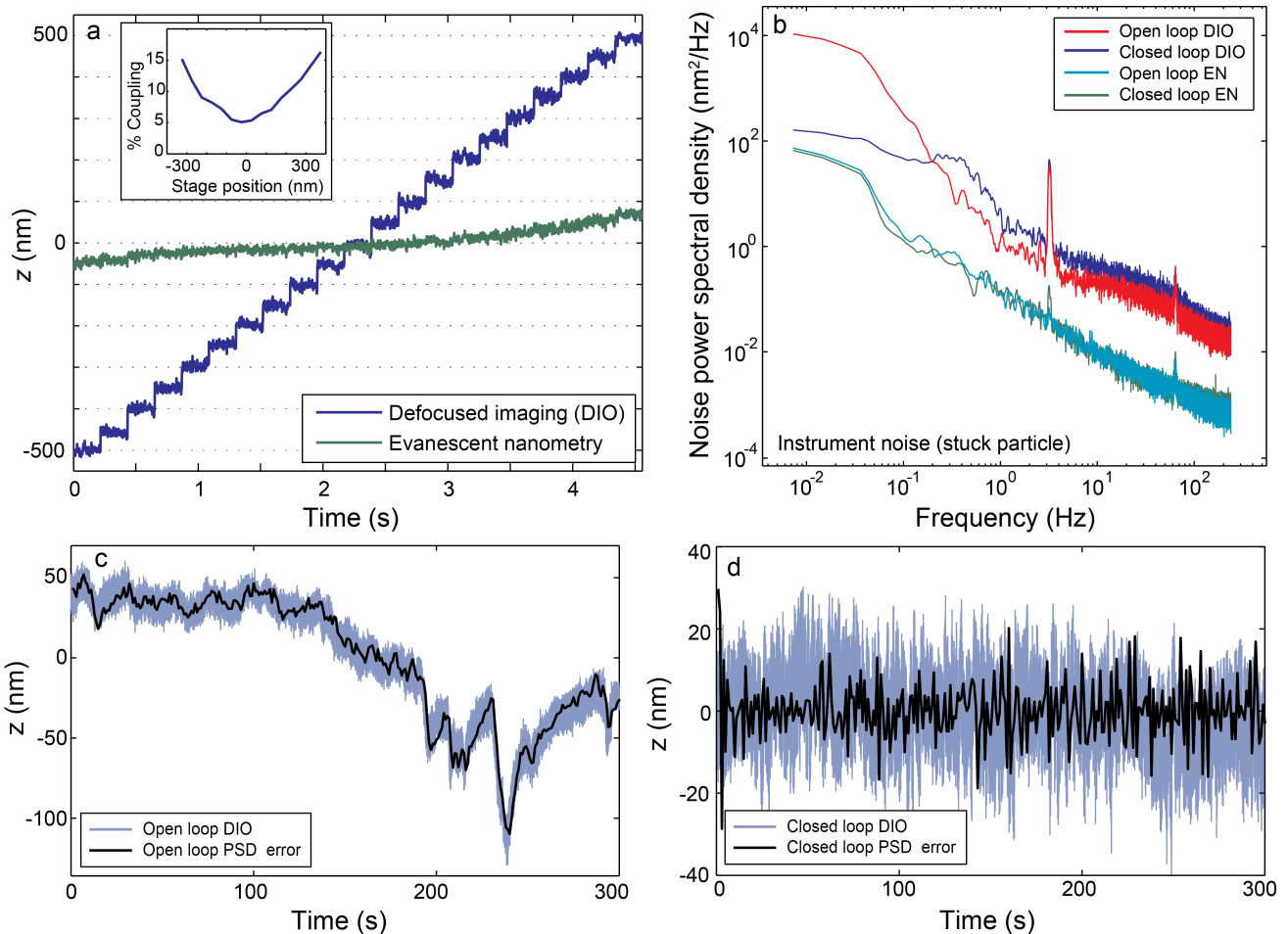
(a) Quantification of evanescent nanometry sensitivity to stage motion. While the sample stage was stepped over a range of +/- 500 nm in 50 nm increments, a rotor bead was simultaneously monitored by DIO and EN. As expected, the DIO signal reproduces the 50 nm steps with high fidelity due to its direct sensitivity to the motion of the stage. However, the EN signal is relatively insensitive to stage motion, and shows an attenuated response. Inset: the derivative of the EN signal with respect to the magnitude of stage motion is shown as a percentage, and plotted as a function of distance from the focus (data shown are averaged over 10 repeats of the 4.5 s calibration sweep). At the optimal focus, the coupling between stage motion and the EN signal is about 5%. **(b)** Noise power spectral density for simultaneous EN and DIO signals acquired fron a surface-bound particle, representing the instrumental noise floor (full-bandwidth standard deviations: DIO, 10 nm; EN, 3 nm). The effect of focus lock can be observed at low frequencies in DIO: some additional noise is introduced around the 1 Hz mark (blue: closed loop DIO), but stability at lower frequencies is improved (compared to red: open loop DIO). EN exhibits lower noise throughout the measurement bandwidth, as well as superior drift rejection. **(c)** Raw DIO and focus lock detector (PSD) error signal of a surface-bound gold nanoparticle. Focus lock typically stabilized the PSD error signal to less than 5 nm (standard deviation). **(d)** In the absence of feedback, the DIO and PSD error signals exhibit well-correlated low frequency noise due to focal drift.

Supplementary Figure 10. Correction of orbit ellipticity.

AuRBT-140nm / 420bp

AuRBT 110nm / 4.1kbp

AuRBT-80nm/4.1kbp

Raw   Corrected
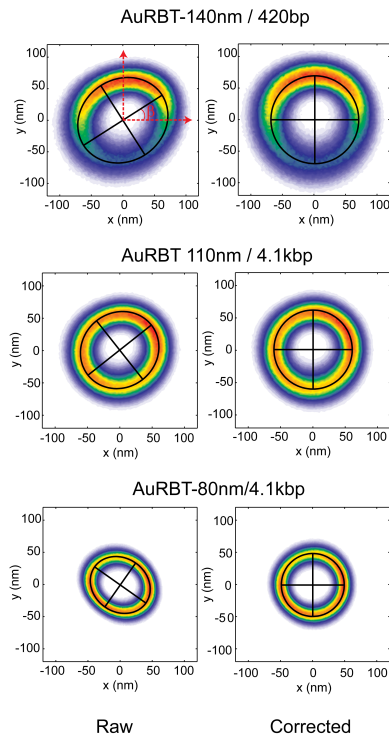
Left column: many rotor beads exhibited some degree of ellipticity in their detected positions during rotation around the DNA. Similar effects have been observed in previous experiments tracking the rotation of gold nanoparticles[17,18], and were corrected by projecting the distribution onto a plane where the orbit is circular. Using a freely available script from the Mathworks (http://www.mathworks.com/matlabcentral/fileexchange/3215-fitellipse), we performed a similar correction by fitting an ellipse to each vector of measured (x,y) positions. Using the extracted eccentricity and orientation angle, a linear transformation was applied to each measured bead position:

$$\begin{bmatrix} x' \\ y' \end{bmatrix} = \begin{bmatrix} \cos\beta & -\sin\beta \\ \sin\beta & \cos\beta \end{bmatrix} \begin{bmatrix} e & 0 \\ 0 & 1 \end{bmatrix} \begin{bmatrix} \cos\beta & \sin\beta \\ -\sin\beta & \cos\beta \end{bmatrix} \begin{bmatrix} x \\ y \end{bmatrix} \quad \text{(S6)}$$

where β is the angle of the ellipse's long axis with respect to the origin, and *e* is the ratio of the short axis to that of the long axis. Right column: corrected bead orbits were circular.

Supplementary Figure 11. Correction of optical anisotropy.
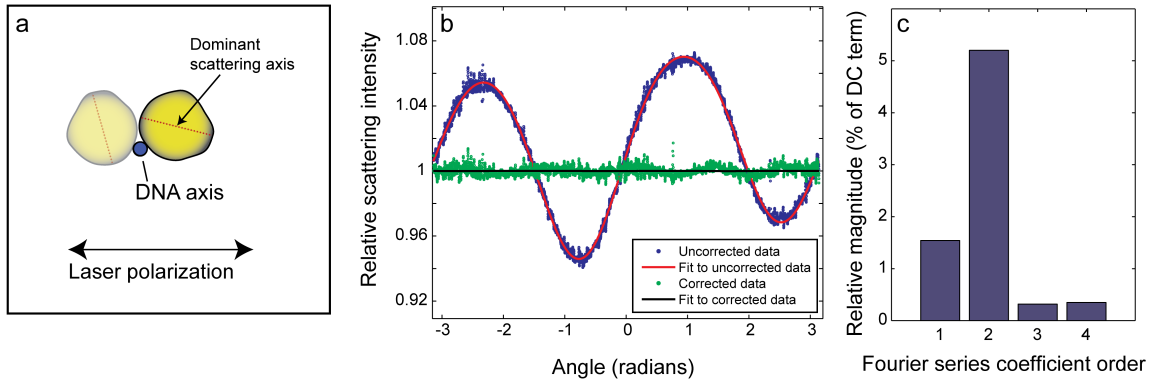
The gold nanoparticles in this study were not optically symmetric[19]: each particle exhibited a rotational signature in which scattering intensity depended on in-plane rotation angle. The effect could be measured and accounted for to eliminate angle-dependent contributions, allowing depth-dependent changes in intensity to be used for evanescent nanometry. **(a)** Anisotropy leads to a modulation in scattering intensity as a function of in-plane angle. The scattering intensity goes up when the dominant axis of the particle is aligned with the polarization of the excitation ("s-polarization" was used, shown here as a horizontal double-sided arrow). **(b)** Modulation profiles were characterized by making a scatterplot of average intensities versus their corresponding in-plane angles [$-\pi,\pi$] (blue) and then analyzed by a 4th order Fourier series decomposition (red):

$$f_4(\phi) = C_o + \sum_{n=1}^{4} C_n \cos(n\phi) + S_n \sin(n\phi) \tag{S7}$$

where the coefficients can be computed directly by integrating the angle-sorted data against corresponding sinusoidal terms, over the domain [$-\pi,\pi$]:

$$C_n = \frac{1}{\pi} \sum_{i=2}^{N} \phi_i \cos(n\phi_i) \delta\phi_i \tag{S8}$$

$$S_n = \frac{1}{\pi} \sum_{i=2}^{N} \phi_i \sin(n\phi_i) \delta\phi_i$$

$$\delta\phi_i = (\phi_i - \phi_{i-1})$$

Summations are over all entries of the angle-sorted trace. The series was limited to fourth order in order to avoid over-correction of the data. Corrected data (green) is flat with respect to particle orientation, and the fit to the corrected data is null. **(c)** Bar graph of the Fourier series coefficient moduli for the data in panel (b), relative to the DC offset. The second order term dominates, suggesting that a dominant dipole scattering axis represents the largest effect.

Supplementary Table 1. Summary of parameters from fits to angular noise power spectral density.
For AuRBT and RBT assays, the table's reported values represent parameters from fits to the datasets in **Fig. 2a** and **Supplementary Fig. 4**. Values for FOMT represent the most favorable numbers reported in ref. 5. *Measured using the DNA tether described in ref. 3. Parameters measured for RBT-300 here are marginally more favorable than those in ref. 3, which used a different rotor bead and assay conditions.

Twist assay	Torsional stiffness, κ (pN nm/rad)	Rotational drag, γ (pN nm s)	Relaxation time, $t_r = \gamma/\kappa$ (ms)	Cutoff frequency, $f_c = \kappa/(2\pi\gamma)$ (Hz)	$S_{f \ll fc} = 4k_BT\gamma/\kappa^2$ (rad^2/Hz)
AuRBT-80nm/420bp	2.46	0.0024	0.98	163	0.0064
AuRBT-140nm/420bp	2.56	0.011	4.4	36	0.028
AuRBT-80nm/4.1kbp	0.28	0.0029	10.1	16	0.58
RBT-300nm/800bp*	1.26	0.162	128	1.24	1.65
Freely Orbiting Magnetic Tweezers (FOMT)[5]	0.27	1.82	6600	0.024	406

Supplementary Table 2. Summary of torque noise power spectral densities and assay parameters.

Torque assay	S_τ, f << f_c ((pN nm)^2/ Hz)	Torsional stiffness, κ (pN nm / rad)	Rotational drag, γ (pN nm s)
Static AuRBT-80nm	0.047	0.28	0.0029
Static AuRBT-110nm	0.15	0.28	0.0093
Static RBT-300nm*	2.6	0.28	0.16
OTW- 500nm[8]	28	264	1.70
eMTT-1μm[13]	146	52	9

*Based on measurements performed in this work using the same particles as reference 15

Supplementary Table 3. Tether construction.

AuRBT tether details

"Bottom constrained" (used for gyrase experiments) — Dig 330 | SGS 420 | TS 7600

"Top constrained" (used for TS-coupling experiments) — LS-D1 | Transducer | F500

"Doubly constrained" (used for static AuRBT) — LS-D6 | SOI | Transducer | F500

☐ Digoxygenin
☐ Biotin
☐ Fluorescein

Segment	Primers	Length	Template	Digest
LS-D1	gcgcgaagacacaatcCGTATCCGCTCACCAAACGCGTTTTTGC <GCAGCGGTTTCTTTACCAGAAGAGT	386	pBiEx-1	Bbs1
LS-D6	GGAAGGAGATTCTCGACAGTTCTAATTGACCTCTTACCTTTTCCCAGTTCAATCTTTGTCAAACACC gtacgaagacaccagtGGGTTCTTCCTAGTGATCTA	388	pFO-2S	Bbs1
Transducer	gaagggtctcatgacTCACTATAGGGCGAATTGGAGCTCCACCGCG gaagggtctcactaaCACTAAAGGGAACAAAAGCTGGGTAC	4156	pFO-SE2	Bsa1
F500	gatcgaagacacttagACAACCCACAAGTATAGAGGCTCCTATG GACGCGGATATAATGACATTTCCTAAC	520	pFO-SE1	Bbs1
Dig 330	gatcgaagacacttagTTACGGATGGCATGACAGTAA AAGTGGTCCTGCAACTTTATCCGCCTC	339	pBiEx-1	Bbs1
SGS 420	gatcgaagacacaatcACCGATTATGGACAGGATTATGCCC ctaagaagactactaaGGATGTGCTGCAAGGCGATTAAG	448	pMS-SGS1	Bbs1
TS 7600	ttgcgaagaccagattTACCTACTTGTCGTCATCGTCCTTG <GACATCAAGAAATAACGCCGGAAC	7624	pLC-M6-898-IQ12	Bbs1

Oligos for SOI

Z50	5' ACTGCCGCTGTACACTCAAGGAAAAGCGCGCGCGCGCGCGCGCGCGCGCGCGCGCGCGCGCGCGCGCGCGCGCAACTTTGGACAACACTCGGCA |||||||||||||||||||||||||||||||||||||||||||||||||||||||||||||||||||||||||||||||||||||||||||||||||||||||||||||||||||||||| 3' GGCGACATGTGAGTTCCTTTTCGCGCGCGCGCGCGCGCGCGCGCGCGCGCGCGCGCGCGCGCGCGCGCGCGCGCGTTGAAACCTGTTGTGAGCCGTACTG

Building blocks for the "Bottom constrained", "Top constrained", and "Doubly constrained" tethers are depicted schematically in the upper box. Primer sequences (including overhangs and enzyme recognition sequences), undigested PCR fragment lengths (bp), template DNA, and restriction enzyme types are shown for all building blocks for the tethers used in this work. Fluorescein modifications are highlighted in red, digoxygenin in yellow, and biotin in green. 5' modifications are shown as angle brackets (<). As described earlier[3,14,20-22], body-labeled segments F500 and Dig 330 were generated by performing PCR reactions with 1/3 of the dTTP replaced with fluorescein-dUTP (Roche) or digoxigenin-dUTP (Roche), respectively. Enzyme recognition sequences are also shown (Bbs1 in cyan, Bsa1 in magenta). Upper case letters indicate template DNA complementarity. The lower box displays the sequence for the 'Z50' SOI insert, which contains the sequence d(pGpC)$_{25}$.

Supplementary Note 1. Calculating the predicted distribution of measured torques. We used a previously described model[14] to fit the $<\tau>(\theta)$ response of Z50 and predict torque distributions. In this model, a sequence of interest (SOI, in this case d(pGpC)$_{25}$) contains N independent basepairs. Each basepair can transition independently from B-DNA to Z-DNA, with associated basepair-normalized changes in equilibrium twist $\Delta\theta_o$, compliance Δc_t, and free energy ΔG_o. Additionally, an energetic penalty J is assessed at each B-Z domain wall. The remainder of the DNA tether contributes only to the overall compliance. The partition function for fixed total twist θ is given by[14]:

$$Z(\theta) = e^{-\beta\frac{1}{2}\kappa_0\theta^2} + \sum_{n=1}^{N}\sum_{d=1}^{\min(n,N-n+1)}\binom{n-1}{d-1}\binom{N-n+1}{d}\sqrt{\frac{\kappa_n}{\kappa_0}}e^{-\beta\left[\frac{1}{2}\kappa_n(\theta-n\Delta\theta_0)^2+n\Delta G_0+2dJ\right]} \tag{S9}$$

where

$$\kappa_n = \frac{\kappa_0}{1+n\Delta c_t\kappa_0} \tag{S9a}$$

and κ_o is the torsional stiffness of the entire molecule in the 100% B-DNA state. We first fit the average torque as a function of imposed twist, using**[14]**:

$$<\tau>(\theta) = -\frac{1}{\beta}\frac{\partial logZ(\theta)}{\partial\theta} = \frac{\kappa_0\theta e^{-\beta\frac{1}{2}\kappa_0\theta^2}+\sum_{n=1}^{N}\sum_{d=1}^{\min(n,N-n+1)}\binom{n-1}{d-1}\binom{N-n+1}{d}\kappa_n(\theta-n\Delta\theta_0)\sqrt{\frac{\kappa_n}{\kappa_0}}e^{-\beta\left[\frac{1}{2}\kappa_n(\theta-n\Delta\theta_0)^2+n\Delta G_0+2dJ\right]}}{Z(\theta)} \tag{S10}$$

To compute the predicted distribution of measured torques, we began by writing a partition function $Z(\psi)$ that considers the lower DNA segment alone, for a given fixed rotor angle ψ. $Z(\psi)$ is given by an identical equation to S9, except that κ_o is replaced by the stiffness κ_{lower} of the lower segment, where:

$$\frac{1}{\kappa_{lower}} = \frac{1}{\kappa_0} - \frac{1}{\kappa_{trans}} \tag{S11}$$

and κ_{trans} is the calibrated stiffness of the upper transducer segment. The probability distribution of rotor angles for a given total imposed twist θ is then given by:

$$P(\psi) = \frac{Z(\psi)e^{-\frac{\beta}{2}\kappa_{trans}(\theta-\psi)^2}}{\int_{-\infty}^{\infty}Z(\psi)e^{-\frac{\beta}{2}\kappa_{trans}(\theta-\psi)^2}d\psi} \tag{S12}$$

The distribution of torques measured from the rotor bead angular displacement is then obtained by a change of variables from the probability distribution of rotor bead angles, using $\tau = \kappa_{trans}(\theta-\psi)$.

Supplementary Note 2. Estimates of optical heating and optical forces.

Laser powers used in this study ranged from 2.5 mW to 80 mW (measured exiting the fiber). After conservatively accounting for known losses, the estimated powers delivered to the sample were at most 1.5 mW – 46 mW. Here we have estimated upper bounds on optical heating and forces for imaging conditions used for all three AuRBT assays.

Calculation parameters:

Wavelength	λ = 845 nm
Beam area	140 μm^2
Field decay length	140 nm
Refractive index of gold at 845nm[23]	n_p = 0.16 + 5.3i
Permittivity of gold	ε_p = -28 + 1.7i
Nanoparticle Radii	R = 40 nm, 55 nm, 70 nm
Refractive index of water	n_w = 1.33
Refractive index of glass	n_g = 1.515
Thermal conductivity of water	K_m = 0.6 W/(m K)

Heating:

Using MATLAB code to evaluate Mie series expansions to fifth order, we estimated scattering and absorption cross sections of the nanoparticles[24]. The temperature rise of the particle can be estimated by balancing the absorbed power with heat dissipation into solution. Assuming steady-state heat transfer, and neglecting convective and radiative modes, the heat generated (left hand side) is equal to the rate of heat conduction into solution (right hand side)[24]:

$$\sigma_{abs}I = 4\pi R^2 K_m \frac{\delta T}{\delta R}$$

At steady-state, the outward heat flow must be equal across a spherical shell of any radius. Hence, the temperature must drop in proportion to r^{-1}, and we can write: $\frac{\delta T}{\delta r} = \frac{\Delta T}{R}$, where ΔT is the temperature rise of the particle compared to the bulk solution temperature, and R is the radius of the particle:

$$\Delta T = \frac{I\sigma_{abs}}{4\pi R K_{water}}$$

Optical forces:

The optical forces on AuRBT's gold nanospheres due to the evanescent field were computed using the method of Bekshaev et al. [25], in which the field is formulated by rotating a plane wave through a complex angle, allowing the scattering fields to be solved using the standard Mie approach; forces are then determined by

integration of the Maxwell stress tensor over a surface surrounding the particle. Axial and lateral forces are calculated for a particle placed directly on the surface.

Results:

	Typical Powers Required for High-Resolution Imaging			Worst Case
	AuRBT-80 nm	**AuRBT-110 nm**	**AuRBT-140 nm**	**AuRBT-140 (excess power)**
Power (from laser)	80 mW	30 mW	2.5 mW	80 mW
Power (at sample, <)	46 mW	17 mW	1.5 mW	46 mW
Intensity	3.3×10^8 W/m^2	1.2×10^8 W/m^2	1.1×10^7 W/m^2	3.3×10^8 W/m^2
Absorption cross-section	1.9×10^{-16} m^2	6.2×10^{-16} m^2	1.6×10^{-15} m^2	1.6×10^{-15} m^2
Scattering cross-section	6.1×10^{-16} m^2	4.9×10^{-15} m^2	2.4×10^{-14} m^2	2.4×10^{-14} m^2
ΔT	0.2°C	0.2°C	0.03°C	1.0°C
F$_{horizontal}$	1.9 fN	4.5 fN	1.7 fN	50 fN
F$_{vertical}$	-8.1 fN	-7.3 fN	-1.2 fN	-35 fN

Conclusion: Heating and forces in AuRBT can generally be neglected. For the worst case condition, in which the highest power is used with the largest particle, heating and forces remain small but could in principle be sufficient to perturb sensitive measurements. Gyrase data included in this study were typically collected using more power than necessary and could be influenced by these small perturbations. However, we recommend to potential practitioners the conservative approach of using no more power than is necessary for imaging.

Supplementary Note 3: Detailed parts list. Essential components required for AuRBT are listed below, with manufacturers. Item labels in bold refer to diagram labels in Supplementary Figure 1. Note that standard mounting hardware components from Thorlabs were used in the setup (parts numbers not listed).

- **EMCCD** camera (Andor iXon+)
- 4 mm **Position Sensitive Detector** (First Sensor DL16-7-PCBA3)
- Data acquisition card (National Instruments PCIe-6323)
- BNC connector block (National Instruments BNC-2090A)
- Inverted microscope body (Nikon Eclipse Ti-S)
- **2.5x** magnifying relay lens (Nikon)
- Oil immersion **objective** (Nikon Apo TIRF objective, NA 1.49 X60)
- Dual view **optical splitter (**Cairn Optosplit II, d)
- XYZ positioning stage (Mad City Labs nano-PDQ)
- High voltage amplifier (Mad City Labs Nanodrive)
- Linear servomotor (Physik Instrumente M-126.PD1)
- Rotary servomotor (Physik Instrumente C-150.PD)
- USB Motor Controller (x2) (Physik Instrumente C-863 Mercury)
- **Fiber-coupled LED** (Thorlabs M660F1)
- **Multimode optical fiber** (Thorlabs M40L01)
- LED current driver (Thorlabs LEDD1B)
- Butterfly laser diode mount (Thorlabs LM142S)
- Laser diode current and temperature controller (Thorlabs ITC4001)
- Imaging lens **L2 (**Thorlabs ITC4001)
- Dielectric mirrors **M1**-**M3** (Thorlabs BB1-EO3)
- Lenses **L3**, **L4** (Thorlabs AC254-100-A-ML)
- Lens **L1** (Thorlabs AC254-500-B-ML)
- DIO lens (Thorlabs AC254-300-A-ML)
- Collimator **C1** (Thorlabs F220FC-B)
- Collimator **C2** (Thorlabs F230SMA-B)
- Irises **I1, I2 (**Thorlabs SM1D12C)
- Zero order half wave plate **HWP** (Thorlabs SM1D12C)
- 45° coupling mirrors **CM1**, **CM2** (Edmund optics #54-0922)
- Fiber-coupled 200mW **845nm single mode diode laser** (Lumics LU0845M200; model discontinued but similar models are available) equipped with a **polarization maintaining fiber** (Corning PM 780)
- 6' x 4' vibration isolation table (TMC)
- Optics mounts and construction hardware (Thorlabs)
- Custom data acquisition computer with 24 Gb RAM, 6-disk highspeed RAID array (Systematic Vision)
- Ultra flat broadband reflecting mirror **M4** (Chroma, z21010)
- 50/50 beamsplitter for DIO (Chroma 21000)
- TIRF filter cube used to house M4 (Chroma 21000)
- Mounting hardware for magnetic tweezers (80/20)
- Rare earth magnets (K&J magnetics B448)
- Recirculating water chiller (Koolance exos-2)
- Custom machined parts used for mounting

Supplementary References

1.   Watanabe, T.M., Sato, T., Gonda, K. & Higuchi, H. Three-dimensional nanometry of vesicle transport in living cells using dual-focus imaging optics. *Biochemical and biophysical research communications* **359**, 1-7 (2007).
2.   Sun, Y., McKenna, J.D., Murray, J.M., Ostap, E.M. & Goldman, Y.E. Parallax: high accuracy three-dimensional single molecule tracking using split images. *Nano letters* **9**, 2676-82 (2009).
3.   Basu, A., Schoeffler, A.J., Berger, J.M. & Bryant, Z. ATP binding controls distinct structural transitions of Escherichia coli DNA gyrase in complex with DNA. *Nat Struct Mol Biol* **19**, 538-46, S1 (2012).
4.   Neuman, K.C. & Nagy, A. Single-molecule force spectroscopy: optical tweezers, magnetic tweezers and atomic force microscopy. *Nature methods* **5**, 491-505 (2008).
5.   Lipfert, J., Wiggin, M., Kerssemakers, J.W., Pedaci, F. & Dekker, N.H. Freely orbiting magnetic tweezers to directly monitor changes in the twist of nucleic acids. *Nature communications* **2**, 439 (2011).
6.   Leach, J. et al. Comparison of Faxen's correction for a microsphere translating or rotating near a surface. *Physical review. E, Statistical, nonlinear, and soft matter physics* **79**, 026301 (2009).
7.   Kestin, J., Khalifa, H. & Correia, R. Tables of the Dynamic and Kinematic Viscosity of Aqueous NaCl Solutions in the Temperature Range 20-150 C and the Pressure Range 0.1-35MPa. *Journal of Physical and Chemical Reference Data* **10**(1981).
8.   Gutierrez-Medina, B., Andreasson, J.O., Greenleaf, W.J., Laporta, A. & Block, S.M. An optical apparatus for rotation and trapping. *Methods in enzymology* **475**, 377-404 (2010).
9.   Sheinin, M.Y., Forth, S., Marko, J.F. & Wang, M.D. Underwound DNA under tension: structure, elasticity, and sequence-dependent behaviors. *Physical review letters* **107**, 108102 (2011).
10.   Deufel, C., Forth, S., Simmons, C.R., Dejgosha, S. & Wang, M.D. Nanofabricated quartz cylinders for angular trapping: DNA supercoiling torque detection. in *Nature methods* Vol. 4 223-5 (2007).
11.   La Porta, A. & Wang, M.D. Optical torque wrench: angular trapping, rotation, and torque detection of quartz microparticles. in *Phys. Rev. Lett.* Vol. 92 190801 (2004).
12.   Ma, J., Bai, L. & Wang, M.D. Transcription under torsion. *Science* **340**, 1580-3 (2013).
13.   Janssen, X.J. et al. Electromagnetic torque tweezers: a versatile approach for measurement of single-molecule twist and torque. *Nano letters* **12**, 3634-9 (2012).
14.   Oberstrass, F.C., Fernandes, L.E. & Bryant, Z. Torque measurements reveal sequence-specific cooperative transitions in supercoiled DNA. *Proceedings of the National Academy of Sciences of the United States of America* (2012).
15.   Oberstrass, F.C., Fernandes, L.E., Lebel, P. & Bryant, Z. Torque Spectroscopy of DNA: Base-Pair Stability, Boundary Effects, Backbending, and Breathing Dynamics. *Physical Review Letters* **110**, 178103 (2013).
16.   Lansdorp, B.M. & Saleh, O.A. Power spectrum and Allan variance methods for calibrating single-molecule video-tracking instruments. *Rev Sci Instrum* **83**, 025115 (2012).
17.   Yasuda, R., Noji, H., Yoshida, M., Kinosita, K., Jr. & Itoh, H. Resolution of distinct rotational substeps by submillisecond kinetic analysis of F1-ATPase. *Nature* **410**, 898-904 (2001).
18.   Furuike, S. et al. Resolving stepping rotation in Thermus thermophilus H(+)-ATPase/synthase with an essentially drag-free probe. *Nature communications* **2**, 233 (2011).
19.   Lehmuskero, A., Ogier, R., Gschneidtner, T., Johansson, P. & Kall, M. Ultrafast Spinning of Gold Nanoparticles in Water Using Circularly Polarized Light. *Nano Lett* (2013).
20.   Gore, J. et al. DNA overwinds when stretched. in *Nature* Vol. 442 836-9 (2006).
21.   Gore, J. et al. Mechanochemical analysis of DNA gyrase using rotor bead tracking. *Nature* **439**, 100-4 (2006).
22.   Bryant, Z. et al. Structural transitions and elasticity from torque measurements on DNA. *Nature* **424**, 338-41 (2003).
23.   P.B. Johnson & Christy, R.W. Optical Constants of the Noble Metals. *Physical Review B* **6**, 4370-4379 (1972).
24.   Dijk, M.A.v. Universiteit Leiden (2007).
25.   Bekshaev, A.Y., Bliokh, K.Y. & Nori, F. Mie scattering and optical forces from evanescent fields: a complex-angle approach. *Opt Express* **21**, 7082-95 (2013).